RESEARCH ARTICLE

Desalination

Energy & Environmental Materials WILEY

# Bioinspired Janus Evaporator for Efficient Desalination of Saline-Alkali and Seawater Through Photothermal-Capillary Effects

*Qi Zhang, Pengfei Zhang*, Shan Song, Chengyu Fu, Limeng Yang, and Cuihong Sheng*

**Soil salinization and freshwater scarcity are critical constraints on sustainable agriculture. Inspired by the salt-resistance mechanisms of *Tamarix chinensis*, this study combined textile technology to ingeniously integrate a hydrophobic PP/MXene photothermal sheath with a hydrophilic cotton core into functionalized yarns, successfully developing a Janus core-sheath evaporator (PM-CSY-F). MXene is uniformly dispersed within the polypropylene matrix, significantly enhancing internal multiple light scattering and interlayer reflections, thereby improving the photothermal conversion efficiency. By precisely regulating the number of cotton cores, the water transport rate can be accurately controlled, achieving synergistic optimization of efficient solar absorption and capillary-driven rapid water transport. The sheath and nighttime radiative cooling enable self-cleaning and suppress salt accumulation. The PP matrix isolates MXene from highly alkaline water, improving stability. Under 1 kW $m^{-2}$ irradiation, the evaporator achieved a 2.34 kg $m^{-2}$ $h^{-1}$ evaporation rate for saline-alkali water (150 M $Na^+$). In simulated seawater, performance improved to 2.46 kg $m^{-2}$ $h^{-1}$. Outdoor tests yielded 12.99 kg $m^{-2}$ of water over 8 h. The textile-based design supports scalable manufacturing. This approach provided a viable solution for both soil remediation and freshwater generation, advancing sustainable agriculture in vulnerable regions.**

## 1. Introduction

The escalating global water scarcity crisis has rendered soil salinization and freshwater shortages critical barriers to sustainable agricultural development.[1–3] Saline-alkali soils occupy approximately 6.5% of the global land area, and saline-alkali water is widely distributed in adjacent regions.[4] This water contaminates surface water during migration and increases salt concentrations in groundwater, exacerbating ecological degradation and water quality risks.[5,6] Existing remediation strategies primarily focus on soil amendments while neglecting simultaneous treatment of saline-alkali water bodies, resulting in inefficient land management.[7–9] This systemic gap highlights the urgent need for integrated "soil–water co-remediation" technologies.

Interfacial solar evaporation has recently demonstrated significant potential for seawater desalination due to its carbon-neutral profile and low energy demands.[10–17] A central research goal is to develop evaporators with high evaporation rates and efficiencies. Photothermal materials—integral to high-performance evaporators—have been widely studied, including semiconductors,[18,19] metallic nanoparticles,[20,21] carbon-based composites,[22,23] and 2D nanomaterials.[24,25] Among these, MXene—a class of 2D transition metal carbides and nitrides—has attracted considerable attention for its mechanical stability, tunable thermal emissivity, and adaptable optical properties.[26–28] MXene has been broadly applied in solar evaporators, showing high desalination performance in previous studies.[29–31]

Conventional solar evaporators face dual challenges when applied to saline-alkali water: Salt Crystallization Dynamics. The solubility of $Na_2CO_3$ and $NaHCO_3$ (21.5 g/100 g and 9.6 g/100 g at 25 °C, respectively) is significantly lower than that of NaCl (35.9 g/100 g), leading to aggravated scaling issues.[14,32] Alkaline Corrosion. Strongly alkaline solutions (pH > 9.0) promote oxidative degradation of photothermal materials.[33–35] To enhance salt resistance, previous studies have introduced superhydrophilic structures and salt backflow channels.[36–40] For example, Su et al.[41] developed a superhydrophobic/superhydrophilic solar interfacial evaporator (SS-SIE) with a superhydrophilic substrate for continuous pumping of hypersaline wastewater and resistance to insoluble organics or oil contamination, a superhydrophobic top layer that enables directional water transport (center → edge) and vertical heat–steam transfer, and salt accumulation confined to the substrate periphery, ensuring long-term operational stability. Wang et al.[42] designed a novel 3D solar crystallizer that employs a dead-end solar-driven mode. The device uses an aluminum sheet with high thermal conductivity to separate the water evaporation surface from the light absorption surface. The bottom and inner walls have high light absorption efficiency (with an absorption rate of 0.99), while the outer wall is used for water evaporation and

Dr. Q. Zhang, Prof. P. Zhang, S. Song, Prof. C. Fu, Prof. L. Yang, Prof. C. Sheng
School of Textile Science and Engineering, Xi'an Polytechnic University, Xi'an 710048, China
E-mail: fengyunjian1981@126.com
Prof. P. Zhang, Prof. C. Fu, Prof. L. Yang, Prof. C. Sheng
Key Laboratory of Functional Textile Material and Product, Xi'an Polytechnic University, Ministry of Education, Xi'an 710048, China
Key Laboratory of Functional Clothing Fabric of Shaanxi Province, Xi'an Polytechnic University, Xi'an 710048, China
The ORCID identification number(s) for the author(s) of this article can be found under https://doi.org/10.1002/eem2.70197.

**DOI: 10.1002/eem2.70197**



© 2026 The Author(s). *Energy & Environmental Materials* published by John Wiley & Sons Australia, Ltd on behalf of Zhengzhou University. This is an open access article under the terms of the Creative Commons Attribution License, which permits use, distribution and reproduction in any medium, provided the original work is properly cited.

salt crystallization. The high thermal conductivity of the aluminum sheet ensures effective heat transfer, which promotes evaporation.[43,44] Despite its effectiveness, this design suffers from complex fabrication and limited scalability, hindering practical application.[45–47] To address these challenges,[48–50] Xu et al.[51] proposed a core-sheath yarn (CSY) strategy that optimizes water pathways to improve desalination efficiency. CSY-based devices, fabricated using conventional textile techniques, offer high scalability and practical utility.[52–58] Integration of textile engineering with superhydrophobic/hydrophilic interfacial design thus presents a viable path to overcoming the salt-resistance bottleneck in evaporator technologies.[59–63]

Inspired by *Tamarix chinensis*, this study proposes a synergistic strategy combining structural and functional biomimicry for efficient desalination of saline-alkali water and seawater. *T. chinensis* maintains a dynamic balance between efficient transpiration and salt secretion through its robust root system and asymmetrically structured stomata. The strong water-transport capacity of its root system and the wax-coated leaf epidermis that reduce salt accumulation inform the design.[64–72] A Janus core sheath evaporator was developed through advanced textile engineering. Its hydrophobic photothermal shell layer (contact angle >100°), which mimics the waxy cuticle of *Tamarix*, not only reduces salt deposition on the surface but also converts solar energy into heat through efficient photothermal conversion. Meanwhile, the hydrophilic core layer, which replicates the xylem vascular bundles, enhances capillary-driven water transport, thereby achieving optimal evaporation conditions. In addition, the polypropylene matrix offers high chemical stability, protecting MXene from degradation under strong alkaline conditions. Polypropylene/MXene composite yarns fabricated via melt-spinning with ultralow MXene loading (2 wt%) exhibited excellent optical performance: 93.4% broadband solar absorption and 91.01% mid-infrared emissivity in the atmospheric window (8–13 μm). This dual-functional material not only achieves efficient solar-thermal conversion during the day but also lowers the surface temperature at night through radiative cooling, further reducing salt deposition. This bioinspired structure transforms passive anti-salinity strategies into active regulation by establishing dual-gradient fields for vapor pressure and ion concentration. These gradients optimize energy and mass transport during brine desalination. The proposed system offers a promising solution for both saline-alkali soil remediation and seawater desalination, supporting sustainable agriculture and water resource management.

## 2. Results and Discussion

### 2.1. Construction and Characterization of PM-CSY and PM-CSY-Based Fabric

Inspired by the morphology of *Tamarix* leaves and traditional textile techniques, this study developed a novel core-sheath structured yarn (CSY) using a polypropylene (PP)/MXene composite as the sheath and cotton fibers as the core for solar interfacial evaporation applications. The preparation process of the evaporator is shown in **Figure 1a**: First, PP and MXene were compounded into yarns via melt-spinning technology; then, using a two-dimensional braiding machine, PM-CSY yarns were prepared with PP/MXene yarns as the sheath and cotton fibers as the core; finally, on a semi-automatic loom, plain-woven CSY-F fabric evaporators were woven with PM-CSY yarns as the warp and PP/MXene yarns as the weft. MXene is uniformly dispersed in the PP matrix, which can enhance the absorption of solar radiation through multiple reflections. By precisely controlling the number of cotton cores, the water transport rate can be accurately controlled, thereby synergistically optimizing light absorption efficiency and capillary-driven water transport performance. Under solar irradiation, photons excite electrons in MXene from the valence band to the conduction band. Subsequently, the excited electrons release energy in the form of phonons through a non-radiative relaxation process, generating localized heat within the material. This heat is further transferred to the interfacial water layer, promoting the conversion of solar energy into thermal energy and ultimately used for the generation of water vapor (as shown in Figure 1b). At night, the high infrared emissivity of the polypropylene matrix endows the evaporator with radiative cooling capabilities, which helps to achieve surface self-cleaning and dissolution of residual salts.

$Ti_3C_2T_x$ MXene nanosheets were synthesized by etching $Ti_3AlC_2$ MAX phase, followed by centrifugation and ultrasonication. Scanning electron microscopy (SEM) revealed mono−/few-layered MXene nanosheets (**Figure 2a**). To achieve homogeneous dispersion of MXene in the PP matrix, solid-phase shear blending was employed to pre-mix freeze-dried MXene nanosheets with PP powder in a high-speed mixer. This process facilitated uniform dispersion and further delamination of multilayered nanosheets. The composite was then melt-spun using a twin-screw extruder to produce PP/MXene composite yarns. Spinning details are shown in Video S1, Supporting Information. The surface morphology of the composite yarn is shown in Figure 2b. Transmission electron microscopy (TEM) confirmed uniform dispersion of MXene in the PP matrix (Figure 2c). High-resolution TEM (HR-TEM) revealed lattice fringe spacing of 0.28 nm, corresponding to the (002) plane of MXene (Figure 2d). SEM cross-sections indicated MXene nanosheets with lateral dimensions of 20–30 μm and thicknesses of 200–300 nm (Figure 2e). Energy-dispersive X-ray spectroscopy (EDS) confirmed homogeneous elemental distribution (C, O, Ti, F) across the yarn cross-section (Figure 2f). The melt-spinning technique enables large-scale production of PP/MXene composite yarns (Figure 2g,h). Mass production of CSYs was achieved using industrial-scale 2D braiding (Figure 2i; Video S2, Supporting Information). The resulting CSY exhibited a core of cotton yarn and a PP/MXene composite sheath (Figure 2j). For fabric production, CSYs were used as warp yarns and PP/MXene yarns as weft yarns to fabricate plain-woven CSY-F fabric on a semi-automatic loom (Figure 2k,l). Both yarns demonstrated compatibility with existing textile machinery, supporting scalability and industrial manufacturability.

The XRD patterns of the constituent materials are presented in **Figure 3a**. The PP matrix displayed characteristic diffraction peaks at 14.2°, 16.9°, 18.6°, 21.2°, and 21.9°, corresponding to the (110), (040), (130), (111), and (131) planes of PP, respectively.[69] No alterations were observed in the crystalline structure of PP following evaporator fabrication, as evidenced by consistent diffraction patterns across all composites. The precursor $Ti_3AlC_2$ showed prominent peaks at 9.45° and 38.89°. After etching, the 9.45° peak shifted to 6.78°, confirming the removal of Al layers and the formation of $Ti_3C_2T_x$ MXene. The presence of the 6.78° peak in the PP/MXene composite yarn (PM-CSY) further confirmed the uniform dispersion of MXene within the PP matrix.

XPS survey spectra (Figure 3b) revealed the elemental composition of MXene, PP, and PM-CSY. All binding energies were calibrated to the C 1s peak at 284.8 eV. Distinct peaks were identified at 284.8 eV (C 1s), 460 eV (Ti 2p), 532 eV (O 1s), and 685 eV (F 1s). Ti and F


© 2026 The Author(s). *Energy & Environmental Materials* published by John Wiley & Sons Australia, Ltd on behalf of Zhengzhou University.

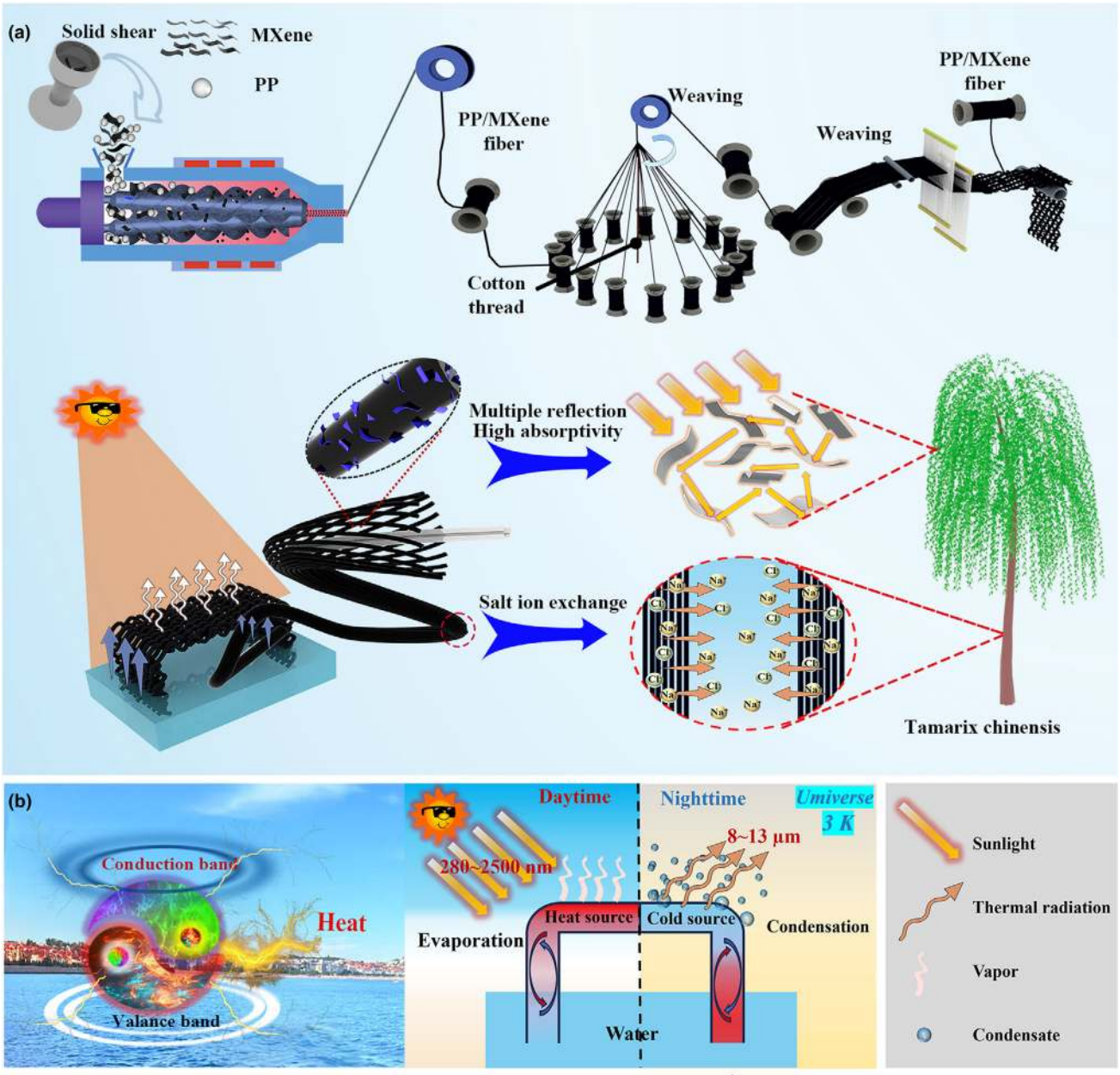



**Figure 1.** Scalability and mass production of core-sheath structured yarns (CSYs) and fabrics (CSY-F). a) Schematic diagram of the CSY and CSY-F fabrication process. b) Schematic diagram of the solar evaporation mechanism.

signals were absent in PP but clearly present in both MXene and PM-CSY, confirming the successful incorporation of MXene into the PP matrix. High-resolution XPS spectra were further analyzed to determine the chemical states of the elements in PM-CSY. The C 1s spectrum (Figure 3d) was deconvoluted into four peaks corresponding to C-Ti (281.4 eV), C=C (282.9 eV), C-C (284.8 eV), and C-O (286.1 eV).[73] The Ti 2p spectrum was resolved into two spin–orbit doublets ($2p_{3/2}$ and $2p_{1/2}$),[74] attributable to the following species: C-Ti-C: 454.5 eV (Ti $2p_{3/2}$) and 460.2 eV (Ti $2p_{1/2}$), C-Ti-O: 455.4 eV (Ti $2p_{3/2}$) and 461.1 eV (Ti $2p_{1/2}$), C-Ti-(O,F): 456.4 eV (Ti $2p_{3/2}$) and 462.2 eV (Ti $2p_{1/2}$), C-Ti-F: 457.6 eV (Ti $2p_{3/2}$) and 463.3 eV (Ti $2p_{1/2}$), $TiO_{2-x}F_{2x}$: 458.7 eV (Ti $2p_{3/2}$) and 464.4 eV (Ti $2p_{1/2}$). The F 1s spectrum included three components: Ti-F (684.4 eV), $TiO_{2-x}F_{2x}$ (685.4 eV), and residual Al-F (686.4 eV). These data confirm the homogeneous dispersion of MXene nanosheets and the preservation of their structural features within the PP matrix throughout the fabrication process.

The chemical stability of PM-CSY under prolonged exposure to saline-alkali water was evaluated by XRD and XPS after 100 h of continuous evaporation (Figure 3e). After continuous evaporation for 100 h, the PM-CSY was washed with deionized water, dried, and then used for testing. The deconvoluted C 1s, Ti 2p, and F 1s spectra showed no significant changes in peak positions or intensities, and no additional peaks were detected. The XRD patterns before and after exposure remained unchanged (Figure 3c), indicating the crystalline structure


© 2026 The Author(s). *Energy & Environmental Materials* published by John Wiley & Sons Australia, Ltd on behalf of Zhengzhou University.

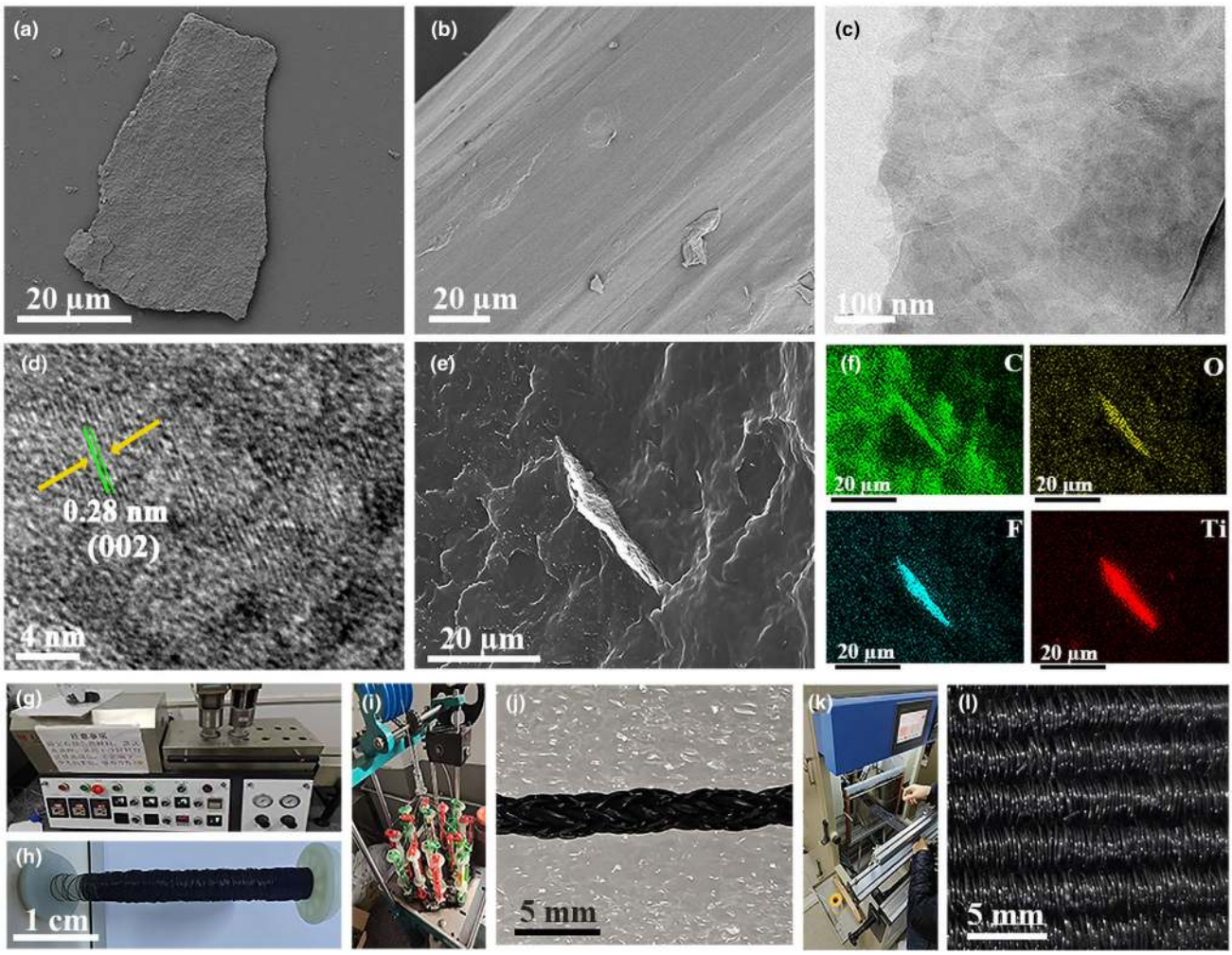



**Figure 2.** Characterization of CSY and CSY-F. a) SEM image of MXene. b) SEM image of PM yarn surface. c) TEM image of PM yarn. d) HR-TEM image of PM yarn. e) SEM image of PM yarn cross-section. f) EDS elemental mapping of PM yarn cross-section. g) Photograph of twin-screw extruder. h) Photograph of PM yarn. i) Photograph of 2D braiding machine. j) Photograph of CSY. k) Photograph of loom used to weave CSY-F. l) Photograph of CSY-F.

was preserved. Raman spectroscopy was employed to characterize the chemical stability of MXene. As shown in Figure S4, Supporting Information, in the MXene $Ti_3C_2T_x$ nanosheets, the peaks at 263 and 609 $cm^{-1}$ correspond to the energy gap modes of in-plane Ti, C, and surface functional group atoms, while the Raman peak at 403 $cm^{-1}$ is attributed to the energy gap modes of in-plane Ti-OH and Ti-O surface functional groups. After 400 hours of evaporation, no significant shifts in the positions of these peaks were observed, nor were any new characteristic peaks detected. Additionally, differential scanning calorimetry (DSC) was used to measure and calculate the thermal properties of polypropylene (PP)/MXene composite yarn before and after 400 hours of saline-alkali water evaporation (see Figure S6, Supporting Information). The testing temperature range was from 30 to 200 °C, with a heating rate of 10 °C/minute. The results indicated that the melting and crystallization temperatures of the PP/MXene composite yarn were 121.2 and 167.1 °C, respectively. After prolonged exposure to saline-alkali water evaporation, no changes in the melting and crystallization temperatures were observed. These results demonstrate that the PP matrix effectively shields the embedded MXene from saline-alkali corrosion, ensuring long-term chemical stability of the composite yarn.

### 2.2. Optical Absorption and Thermal Management Performance of PM-CSY-F

**Figure** 4a illustrates the mechanism of solar-driven interfacial evaporation in semiconductor materials. Under solar irradiation, photons with sufficient energy excite electrons from the valence band (VB) to the conduction band (CB).[69] Relaxation of these electrons to lower energy states releases energy as phonons, inducing localized heating of MXene. This heat is transferred to surface water via non-radiative processes, resulting in evaporation and completing the solar–thermal–vapor conversion cycle.

The absorption spectrum of PM-CSY-F across the entire solar spectrum is shown in Figure 4b (gray curve: AM 1.5 global solar spectrum). Solar absorptivity ($A$) was calculated using Equation (1):


© 2026 The Author(s). *Energy & Environmental Materials* published by John Wiley & Sons Australia, Ltd on behalf of Zhengzhou University.

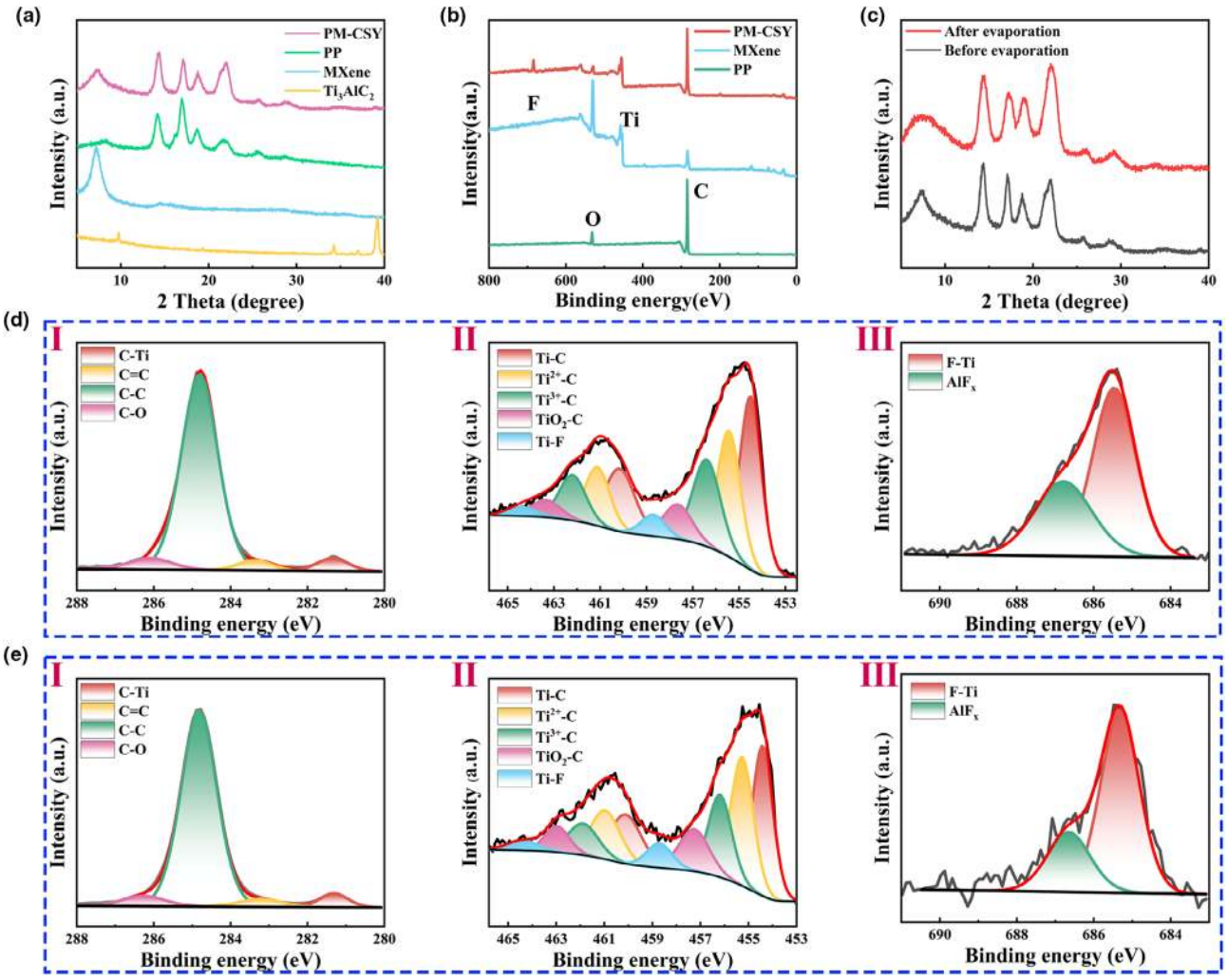



**Figure 3.** Interactions among PM-CSY components. a) XRD patterns of $Ti_3AlC_2$, MXene, PP, and PM-CSY. b) XPS spectra of MXene, PP, and PM-CSY. c) XRD patterns of PM-CSY before and after evaporation. d) XPS spectra of C 1s, Ti 2p, and F 1s in PM-CSY before evaporation. e) XPS spectra of C 1s, Ti 2p, and F 1s in PM-CSY after evaporation.

$$A = 1 - R - T \quad (1)$$

where R and T represent the solar reflectance and transmittance, respectively (see Figure S8, Supporting Information). The light absorption performance of the polypropylene/MXene composite across a broad spectrum (280–2500 nm) increases first and then decreases with the increase of MXene loading, reaching a peak at a loading of 2%, with values ranging from 88.6% to 95.5% and an average of 93.4% (see Figure S9, Supporting Information). Compared with MXene film (51.6%, Figure S11, Supporting Information), the absorption rate of the composite material is significantly improved. The reasons are as follows: the film surface has direct reflection losses, while the dispersed distribution of MXene in the PP matrix induces multiple internal reflections, which fully capture sunlight. After the incident photons are absorbed by MXene, the excited electrons transition from the valence band to the conduction band. Subsequently, the electrons relax and release phonons, and the energy is quickly converted into localized heat, realizing efficient photo-thermal conversion.[69]

Surface temperatures of PM-CSY-F under dry and wet conditions were recorded using an infrared thermal camera under 1 kW $m^{-2}$ solar illumination (Figure 4c). After 300 s, surface temperatures stabilized at ~75 °C (dry) and ~38 °C (wet), confirming strong light absorption. COMSOL Multiphysics simulations reproduced the heating process, predicting surface temperatures of ~74.5 °C (dry) and ~37.6 °C (wet) after 5 min (Figure 4d). The simulation results showed deviations of only ~0.5 and ~0.4 °C from experimental data, validating the heat transfer model. These results confirm the evaporator's excellent thermal localization and insulation, which reduce heat loss and improve energy utilization.

Figure 4e shows the infrared emissivity spectrum of the composite fabric, which ranged from 85.5% to 95.4% (average: 91.01%) within the atmospheric transparency window (8–13 μm). This high emissivity is attributed to the strong vibrational modes of the PP matrix molecular chains and side groups. Efficient full-spectrum solar absorption supports photothermal conversion during the day, while high mid-infrared emissivity enables passive radiative cooling by dissipating heat to the cold sky. In a windless environment at 25 °C with a relative humidity


© 2026 The Author(s). *Energy & Environmental Materials* published by John Wiley & Sons Australia, Ltd on behalf of Zhengzhou University.

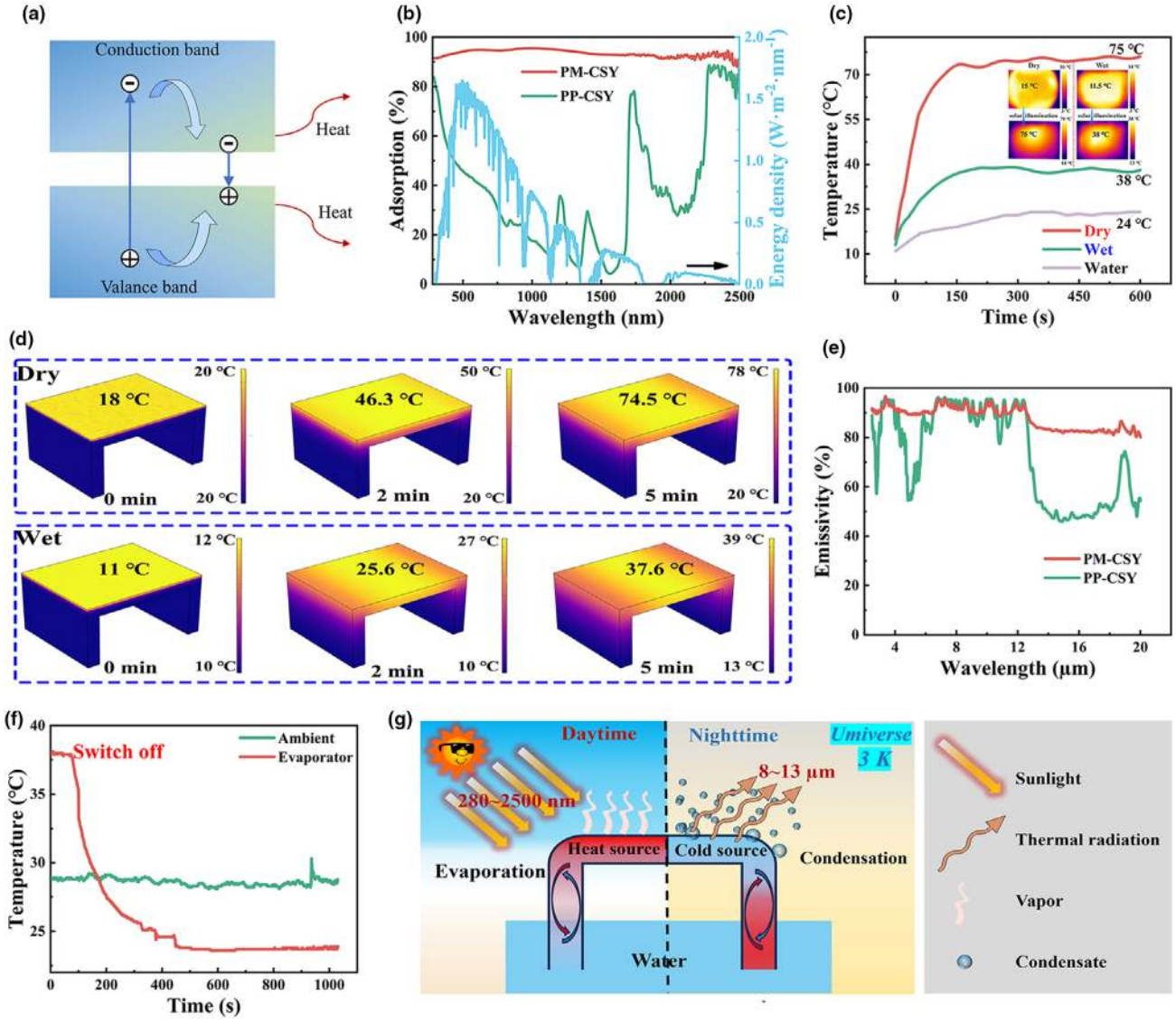



**Figure 4.** Hydrophilicity, light absorption, and thermal management properties of PM-CSY-F. a) Schematic illustration of the solar-driven interfacial evaporation mechanism of semiconductor-based materials. b) Absorption spectrum of the fabric across the full solar spectrum; gray curve represents the AM 1.5 global solar spectrum. c) Temperature difference of the PM-CSY-F evaporator in wet and dry states. d) Surface temperature evolution of the PM-CSY-F evaporator in wet and dry states over 5 min, simulated using COMSOL. e) Infrared emission spectra of the fabric. f) Temperature change of the PM-CSY-F evaporator in the dark. g) Schematic of the evaporation process of the PM-CSY-F fabric under day/night conditions.

of 30%, the surface temperature of the PM-CSY-F evaporator rapidly rises to approximately 37.6 °C under 1 sun illumination. After the light source is removed, the temperature quickly drops and stabilizes at around 6 °C below the ambient temperature (Figure 4f), which fully demonstrates the high efficiency of nighttime radiative cooling. The dual-function evaporative mechanism is summarized in Figure 4g. During the day, photons excite electrons to the CB, followed by non-radiative relaxation that heats MXene and adjacent water, promoting evaporation. At night, the composite's high infrared emissivity allows for effective radiative cooling, reducing surface temperature to ~6 °C below ambient. This promotes atmospheric water condensation on the fabric surface, maintaining hydration and enabling a self-cleaning effect by dissolving and removing residual salts.

### 2.3. Hydrophilicity, Salt Resistance, and Self-Cleaning Properties of PM-CSY-F

To achieve high evaporation rates and maintain self-cleaning capabilities, the wettability of the material was assessed via water contact angle (WCA) measurements of the core-layer cotton yarn and sheath-layer PM yarn in the core-sheath structured yarn (CSY). As shown in **Figure 5a**, the cotton core exhibited hydrophilic behavior, with water droplets rapidly penetrating its surface, ensuring a continuous water supply to the liquid–vapor interface. In contrast, the PM sheath displayed a hydrophobic WCA of 100°, forming a Janus structure. This asymmetric wettability effectively suppressed salt accumulation on the evaporator surface, thereby maintaining stable evaporation rates.


© 2026 The Author(s). *Energy & Environmental Materials* published by John Wiley & Sons Australia, Ltd on behalf of Zhengzhou University.

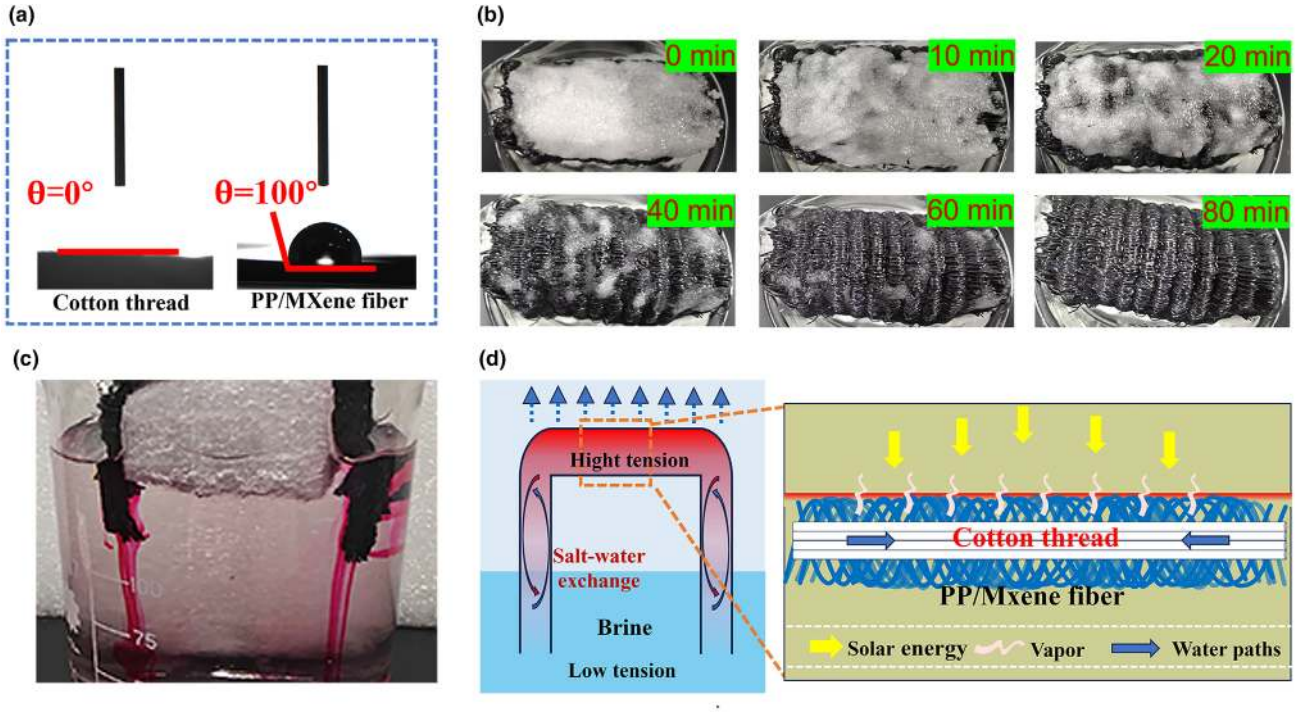



**Figure 5.** Hydrophilicity, salt tolerance, and self-cleaning properties of PM-CSY-F. a) Water contact angle (WCA) images of cotton thread and PM yarn. b) Digital photos showing salt dissolution. c) Digital photos demonstrating diffusion and convection-driven flow of high-concentration saltwater toward low-salinity saltwater. d) Schematic diagram of the salt-water exchange process.

PM-CSY-F exhibited strong anti-fouling and self-cleaning performance under prolonged solar irradiation. The surface of the PP/MXene sheath was characterized using Atomic Force Microscopy (AFM), as shown in Figure S14, Supporting Information. The results revealed that the sheath surface has micro- and nano-scale roughness. This micro-nano structure can significantly increase the contact angle between the liquid and the fiber surface. For hydrophobic surfaces (contact angle $>90°$), an increase in surface roughness will further increase the contact angle, thereby significantly enhancing the hydrophobicity. Therefore, the micro-nano structure on the fiber surface endows the sheath with good hydrophobicity, effectively preventing the adsorption of seawater on the fiber surface, and thus providing excellent salt resistance. When 5 g of solid NaCl was placed directly on the evaporator surface, complete dissolution occurred within 80 min under 1-sun illumination (Figure 5b). To more clearly observe the salt transport pathways in PM-CSY-F, NaCl stained with red dye was evenly spread over the surface of the evaporator. The diffusion of salt from the evaporator to the bulk solution and the convection-driven flow of concentrated brine were observed and recorded. Salt resistance in PM-CSY-F originates from its core-sheath architecture. The cotton core ensures regulated water transport via capillary action, while the hydrophobic PP-MXene sheath facilitates efficient solar-to-thermal conversion. This design sustains continuous water delivery to the evaporation interface and promotes ion exchange along the water transport channels. During evaporation, a concentration gradient forms at the interface. As saturation is approached, the resulting chemical potential difference drives dissolved salt ions back into the bulk brine (Figure 5d). This dynamic ion redistribution suppresses surface crystallization and supports long-term desalination performance.[51]

## 2.4. Evaporation Performance of PM-CSY-F Evaporator

### 2.4.1. Saline-Alkali Water Purification

**Figure 6**a presents a side-view image of the core-sheath structured yarn (CSY) evaporator, showing its tightly interwoven architecture. This configuration enhances light absorption via zigzag reflection pathways. In the PM-CSY-F evaporator, multiple factors influence evaporation performance. Real-time mass changes were recorded using a high-precision electronic balance (accuracy: 0.1 mg) connected to a computer (Figure 6b). As shown in Figure 6c, under 1-sun illumination, PM-CSY-F evaporators with identical water supply cores but varying MXene contents (0%, 0.5%, 1%, 2%, and 3%) achieved evaporation rates of 1.01, 1.5, 2.01, 2.34, and 2.3 $kg\,m^{-2}\,h^{-1}$, respectively.

Significantly higher than the pure water evaporation rate of 0.51 $kg\,m^{-2}\,h^{-1}$. The rate increased with MXene content up to 2%, then declined. Uniformly dispersed MXene improved solar absorption via internal reflections. However, excessive loading ($>2\%$) caused particle aggregation in the PP matrix, which hindered reflection and reduced photothermal efficiency. As shown in Figure S9, Supporting Information, the light absorption performance first increases and then decreases with the increase of MXene content, reaching a peak at a loading of 2%. This finding further confirms that the uniform dispersion of MXene within the polypropylene matrix significantly enhances internal multiple light scattering and interlayer reflections, thereby increasing the light absorption efficiency.

Evaporators with varying numbers of water supply channels (cotton cores) were also tested under 1-sun illumination. As shown in Figure 6d, the evaporation rates for devices with 0, 2, 4, 6, and 8 cores


© 2026 The Author(s). *Energy & Environmental Materials* published by John Wiley & Sons Australia, Ltd on behalf of Zhengzhou University.

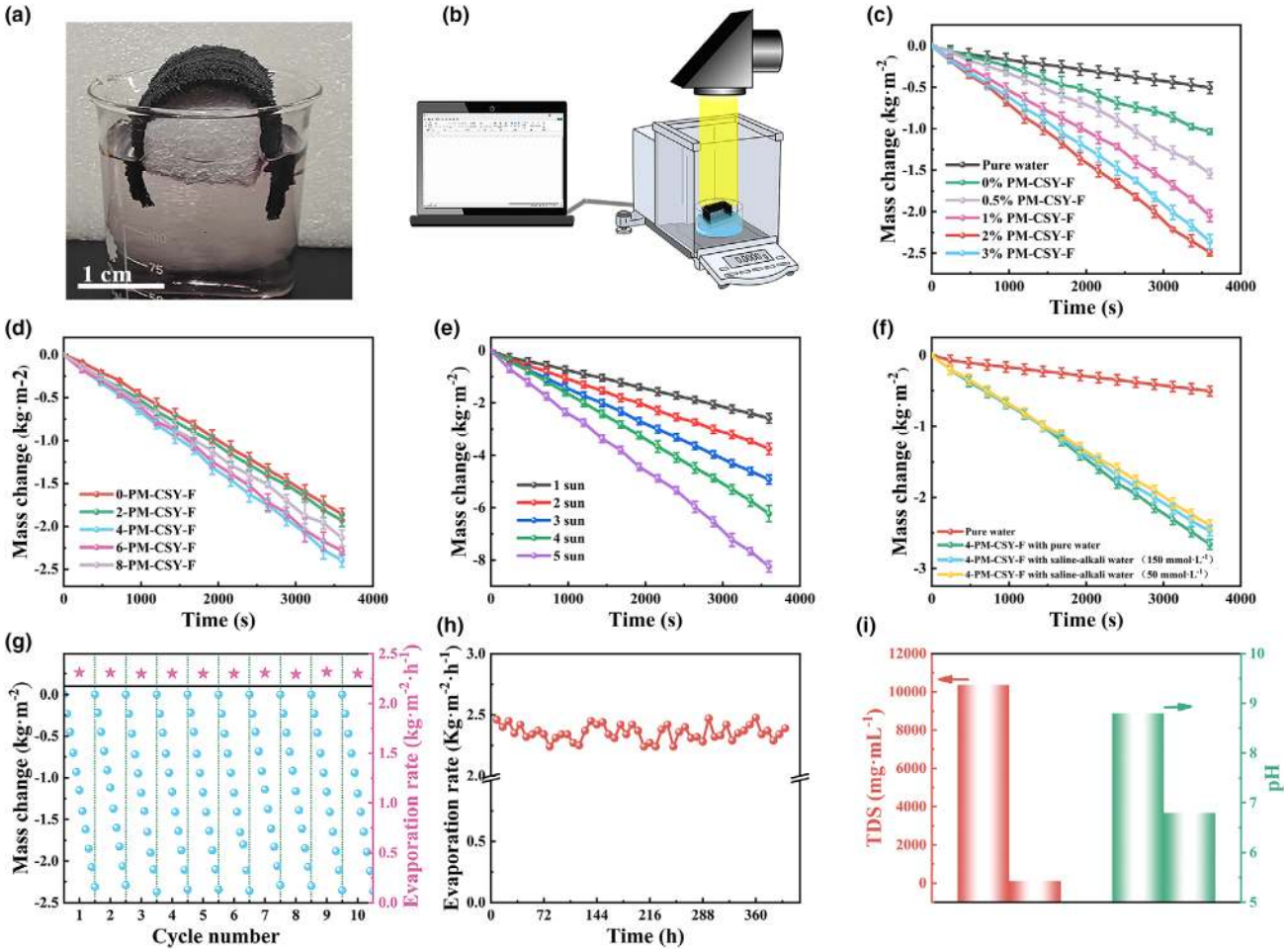



**Figure 6.** Saline-alkali water purification performance of the CSY-F evaporator. a) Side-view photograph of the PM-CSY-F evaporator. b) Schematic diagram of the solar evaporation experimental setup. c) Mass loss of CSY-F evaporators with different MXene contents under 1-sun illumination for treating high-salinity alkali water (150 mmol $L^{-1}$ $Na^{+}$). d) Mass loss of CSY-F evaporators with varying numbers of core yarns under 1-sun illumination for treating high-salinity alkali water (150 mmol $L^{-1}$ $Na^{+}$). e) Evaporated water mass changes of the CSY-F evaporator under 1–5 sun illumination intensities. f) Time-dependent mass loss during liquid evaporation under 1-sun illumination. g) Evaporation rate variations during 10 cyclic desalination tests of the CSY-F evaporator in saline-alkali water (150 $mmol^{-1}$ $Na^{+}$) under 1-sun illumination. h) Continuous evaporation rate measured over 400 h under 1-sun illumination. i) Comparison of total dissolved solids (TDS) and pH of saline-alkali water (150 mmol $L^{-1}$ $Na^{+}$) before and after purification.

were 1.81, 1.88, 2.34, 2.25, and 2.07 kg $m^{-2}$ $h^{-1}$, respectively. The increase followed by a decline indicates an optimal balance between capillary-driven transport and heat loss. As shown in Figure S17, Supporting Information, with the increase in the number of water supply channels, the rate of water transport also increases. Faster water transport is conducive to the evaporation process of the evaporator, thereby increasing the evaporation rate. However, when the water transport is too fast, it will carry away some of the heat used for evaporation, resulting in a decrease in the evaporation rate. Therefore, the configuration with 4 cores (4-PM-CSY-F) offered optimal water management.

Figure 6e shows the evaporation rates of 4-PM-CSY-F under varying illumination intensities (1–5 suns), which reached 2.34, 3.62, 4.81, 6.15, and 8.13 kg $m^{-2}$ $h^{-1}$, respectively. The linear trend confirms excellent light responsiveness and thermal management. Even under 5-sun conditions, the evaporator maintained stable performance. The solar-to-vapor conversion efficiency (η) of 4-PM-CSY-F was calculated using the following equations:[74]

$$\eta = \frac{V_n(H_{lv} + Q)}{E_i} \quad (2)$$

$$H_{lv} = 1.91846 \times 10^6 \times \left(\frac{T_a}{T_a - 33.91}\right) \quad (3)$$

$$Q = c \times (T_a - T_i) \quad (4)$$

where $V_n$ is the net evaporation rate (kg $m^{-2}$ $h^{-1}$), $H_{lv}$ is the latent heat of vaporization (J $kg^{-1}$), $Q$ is the sensible heat (J $kg^{-1}$), Ei is the incident solar energy (kJ $m^{-2}$ $h^{-1}$), $c$ is the specific heat capacity of water (4.2 J $g^{-1}$ $K^{-1}$), $T_a$ is evaporation temperature (K), and $T_i$ is the initial water temperature (K). The calculated η reached 147.6%. The evaporator exhibits a high efficiency of solar-to-water vapor energy conversion, which is mainly attributed to the efficient confinement of local heat and the effective utilization of environmental energy.[74] In addition to directly absorbing solar


© 2026 The Author(s). *Energy & Environmental Materials* published by John Wiley & Sons Australia, Ltd on behalf of Zhengzhou University.

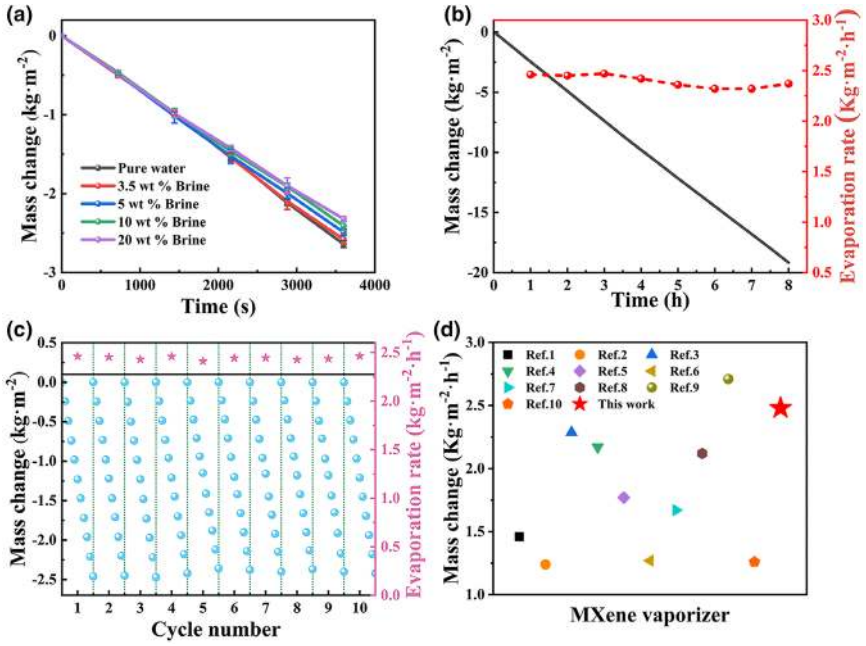



**Figure 7.** Seawater purification performance of the CSY-F evaporator: a) Mass change of evaporated water under different brine salinities under 1-sun illumination. b) Continuous evaporation rate over 8 h. c) Evaporation rate during 10 cyclic evaporation tests. d) Comparison with other MXene-based evaporators.

energy, the composite material shows a high emissivity of 85.5% to 95.4% in the atmospheric window region (8–13 μm wavelength band) due to the significant molecular chain vibrations and side-group structures of the polypropylene (PP) matrix, with an average emissivity as high as 91.01%. Under the condition of thermal steady-state,[69] the emissivity is equal to the absorptivity, which means that the absorptivity of the atmospheric window can reach 91.01%. This characteristic enables the evaporator to fully utilize the energy in the atmospheric window to further promote the evaporation of water.

Durability and long-term stability were evaluated under high salinity–alkalinity conditions (150 M $Na^+$). As shown in Figure S25, Supporting Information, the 4-PM-CSY-F evaporator maintained a stable evaporation rate with no visible salt accumulation after 8 h of continuous operation. Cyclic desalination tests (Figure 6g) showed consistent evaporation behavior across cycles, with a rate maintained at ~2.34 kg $m^{-2}$ $h^{-1}$. These results indicate effective interfacial desalination during the day and passive salt rejection at night, confirming self-regenerating performance. As shown in Figure 6h, after 50 cycles over 400 h (each cycle: 8 h illumination, 16 h rest), the 4-PM-CSY-F maintained high and stable evaporation performance. As shown in Figure S22, Supporting Information, after 400 h of continuous evaporation, salt accumulation appeared on the surface of the evaporator, and the evaporation rate showed a downward trend. Through the above comparative experiments, we further confirmed that the nighttime cooling mechanism can effectively remove the salt accumulation on the surface of the evaporator, thereby maintaining the efficiency and stability of its evaporation performance. Figure 6i further demonstrates its purification capacity. The total dissolved solids (TDS) of the evaporated water were reduced to 100 mg $L^{-1}$, comparable to deionized water. This corresponds to a 99.03% removal rate. The pH of the collected water was also substantially lower than that of the feed saline-alkali water, indicating effective removal of alkaline components. These findings confirm that the solar-driven 4-PM-CSY-F evaporator offers high efficiency, excellent durability, and strong potential for saline–alkali water treatment.

### 2.4.2. Seawater Desalination

The seawater desalination performance of the 4-PM-CSY-F evaporator was systematically evaluated. As shown in **Figure 7**a, the evaporator exhibited high evaporation rates in pure water and NaCl solutions of increasing salinity: 2.61, 2.54, 2.46, 2.37, and 2.30 kg $m^{-2}$ $h^{-1}$ for 0%, 3.5%, 5%, 10%, and 20% (wt%) NaCl, respectively. These results demonstrate robust performance across a wide salinity range. A continuous evaporation test using a 3.5% NaCl solution (simulated seawater) was conducted in the laboratory. As shown in Figure 7b, the 4-PM-CSY-F evaporator maintained a stable evaporation rate over 8 h of operation, indicating excellent durability and operational stability.

Ten-cycle evaporation tests were further performed using 3.5% and 20% NaCl solutions (Figure 7c and Figure S20, Supporting Information). The evaporator achieved an average rate of 2.46 kg $m^{-2}$ $h^{-1}$ in 3.5% brine with a solar-to-vapor efficiency of 154.6%. Even at 20% salinity, it maintained an average rate of 2.30 kg $m^{-2}$ $h^{-1}$ and an efficiency of 144.6%, with no evidence of salinity-induced degradation. The CSY-F evaporator outperformed most reported MXene/Fabric-based photothermal evaporators in terms of evaporation rate (Figure 7d and Figure S23, Supporting Information).[75–84] In addition, the evaporator's compatibility with scalable textile manufacturing processes supports its feasibility for practical, large-scale applications.

## 2.5. Practical Application of CSY-F Evaporator

To assess real-world performance, the 4-PM-CSY-F evaporator was tested outdoors under natural sunlight. Large-scale PM-CSY-F evaporators were fabricated using standard industrial weaving techniques (**Figure 8**a,b). The outdoor test setup (Figure 8c) included a transparent PMMA condensation chamber designed to collect freshwater. The chamber featured a sloped acrylic roof with a central partition. Seawater and the evaporator were placed on one side, while condensed vapor droplets collected on the opposite side for retrieval (Figure 8c). During the test (9:00–17:00), ambient temperature, surface temperature, solar irradiance, and freshwater mass were continuously recorded. As shown in Figure 8d, the evaporator's surface temperature fluctuated in accordance with sunlight intensity, stabilizing at ~35 °C—higher than ambient conditions. Over the 8-h period, the system yielded 12.99 kg $m^{-2}$ of freshwater (Figure 8e). Although this rate was lower than laboratory measurements, the difference was due to lower outdoor solar irradiance.

Natural seawater collected from the Yellow Sea (Qingdao, China) was desalinated using the 4-PM-CSY-F evaporator. Post-purification,


© 2026 The Author(s). *Energy & Environmental Materials* published by John Wiley & Sons Australia, Ltd on behalf of Zhengzhou University.

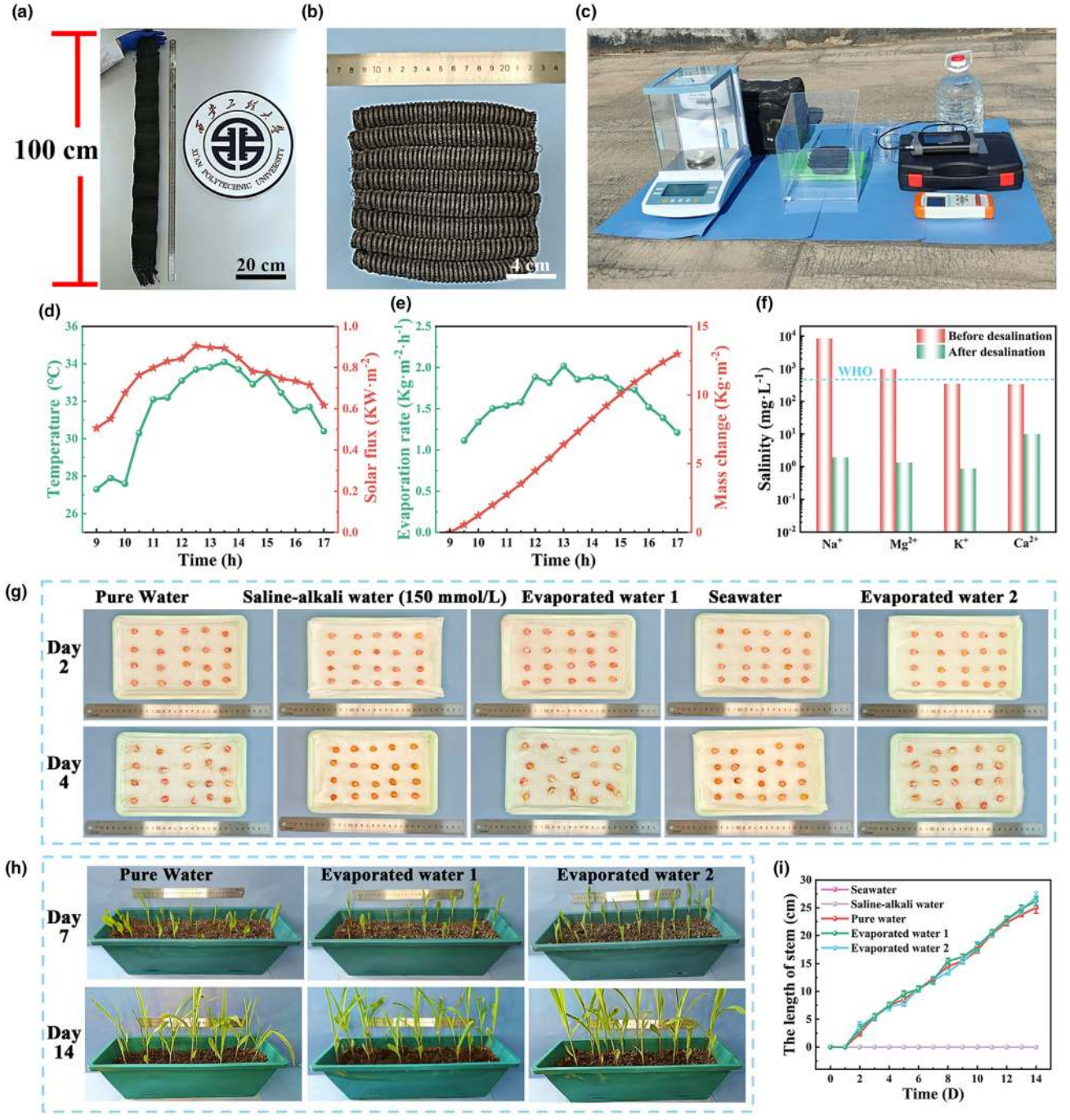



**Figure 8.** Outdoor application of the PM-CSY-F evaporator: a) Photograph of the large-scale evaporator. b) PM-CSY-F-based fabric evaporator. c) Outdoor "evaporation-condensation-collection" device. d) Ambient temperature and solar irradiance during testing. e) Evaporation rate and cumulative water production. f) Changes in metal ion concentration pre- and post-treatment. g) Maize germination under different water treatments. h) Maize seedling growth. i) Time-dependent variation in maize stem length.

the concentrations of $Ca^{2+}$, $K^{+}$, $Mg^{2+}$, and $Na^{+}$ were analyzed via inductively coupled plasma optical emission spectroscopy (ICP-OES). As shown in Figure 8f, ion concentrations in the purified water were significantly reduced and complied with World Health Organization (WHO) standards for drinking water salinity. These findings confirm that the 4-PM-CSY-F-based system effectively produces potable freshwater from seawater via photothermal interfacial evaporation.

To assess the phytotoxicity of the desalinated water, maize seed growth was monitored under five irrigation conditions: pure water (PW), saline-alkali water (SAW), evaporated water from SAW (EW1), seawater (SW), and evaporated water from SW (EW2). Growth


© 2026 The Author(s). *Energy & Environmental Materials* published by John Wiley & Sons Australia, Ltd on behalf of Zhengzhou University.

parameters, including stem length and germination rate, were recorded. Figure 8g shows seedling development over time. Seeds irrigated with PW, EW1, and EW2 germinated successfully, while those in SAW and SW failed to grow (Figure 8h). Stem lengths in the PW, EW1, and EW2 groups were comparable, indicating normal early-stage development (Figure 8i). In contrast, the SAW and SW groups showed no germination due to high salinity. Germination rates (Figure S26, Supporting Information) were 96% (PW), 94% (EW1), and 95% (EW2), compared with 0% for SAW and SW. These results demonstrate that the PM-CSY-F evaporator produces desalinated water suitable for plant irrigation and growth. The system enables practical remediation of saline-alkali soils and supports agricultural applications, particularly in water-scarce or ecologically stressed regions.

## 3. Conclusions

This study developed a Janus core-sheath evaporator (PM-CSY-F) with asymmetric wettability via biomimetic design for efficient desalination of saline-alkali water and seawater. The evaporator incorporates salt-tolerant features of *Tamarix chinensis* and utilizes textile fabrication to integrate functionalized yarns, enabling synergistic enhancement of photothermal conversion and capillary-driven water transport. Under 1 kW $m^{-2}$ solar irradiation, PM-CSY-F achieved an evaporation rate of 2.34 kg $m^{-2}$ $h^{-1}$ for saline-alkali water (150 mmol $L^{-1}$ $Na^{+}$), reducing total dissolved solids (TDS) from 10 364 mg $L^{-1}$ to 100 mg $L^{-1}$, with a stabilized pH of 6.8 ± 0.3. In simulated seawater (3.5 wt% NaCl), the evaporation rate increased to 2.46 kg $m^{-2}$ $h^{-1}$. An 8-h outdoor test demonstrated a daily yield of 12.99 kg $m^{-2}$. The hydrophobic photothermal sheath inhibited salt deposition, while the PP matrix protected the embedded MXene from degradation in alkaline environments. The hydrophilic core replicated xylem-like capillary water transport, significantly enhancing water supply to the evaporative interface. This biomimetic design transforms salt resistance from passive to active regulation by constructing dual-gradient fields for vapor and salt ions, improving energy and mass transfer during desalination. The scalable, textile-based evaporator offers a practical route for rehabilitating saline-alkali soils and securing irrigation water, supporting sustainable agriculture in ecologically vulnerable regions.

## 4. Experimental Section

*Materials:* Hydrochloric acid (37%) from Shanghai Aladdin Biochemical Technology Co., Ltd. LiF was purchased from Shanghai Macklin Biochemical Co., Ltd., $Ti_3AlC_2$ powder (400 mesh) was provided by Newene Technology Co., Ltd., and PP powder (homopolymer, melt index 35 g/10 min) was purchased from Shanghai Macklin Biochemical Co., Ltd. All chemicals were used without any pretreatment.

*Fabrication of CSY:* *Synthesis of MXene*—Lithium fluoride (LiF, 1.8 g) was dissolved in hydrochloric acid (HCl, 20 mL) and stirred at room temperature. After 10 min, titanium aluminum carbide ($Ti_3AlC_2$, 1.0 g) was gradually added. The mixture was stirred continuously at 35 °C for 24 h. The etched suspension was washed with deionized (DI) water 8–10 times via centrifugation until the supernatant reached pH 6. The resulting clay-like sediment (Figure S2, Supporting Information) was dispersed in DI water (150 mL) and ultrasonicated for 1 h. The dispersion was centrifuged at 3500 rpm for 5 min, and the supernatant containing $Ti_3C_2T_x$ MXene (Figure S4, Supporting Information) was collected and freeze-dried to obtain MXene powder.

*Fabrication of PP/MXene yarns*—Polypropylene (PP) powder and freeze-dried MXene were pre-mixed via solid-phase shear blending in a high-speed mixer to ensure homogeneous dispersion. The mixture was melt-extruded at 175 °C using a twin-screw extruder to form continuous PP/MXene filaments. These filaments were stretched at 0.1 km $min^{-1}$ to reduce diameter and enhance mechanical strength. Pure PP yarns and PP/MXene (PM) composite yarns were prepared using identical procedures for comparative analysis.

*Fabrication of CSY*—CSYs were produced through two-dimensional (2D) braiding, in which PM composite yarns were interlaced with sheath yarns around a cotton yarn core (40 tex) to create a hierarchical structure. The parameters of the twister were as follows: 1 hollow spindle speed = 3000 revolutions per minute (r $min^{-1}$); 2 front roller speed = 10.07 m $min^{-1}$; 3 ring spindle speed = 1400 r $min^{-1}$; 4 middle front roller speed = 1.95 m $min^{-1}$; 5 delivery roller speed = 6.67 m $min^{-1}$; and 6 middle rear roller speed = 1.30 m $min^{-1}$. CSYs with varying core-sheath ratios were fabricated by adjusting the number of core yarns: 0-PM-CSY, 2-PM-CSY, 4-PM-CSY, 6-PM-CSY, 8-PM-CSY, and 4-PP-CSY (pure PP core control).

*Fabrication of textile-based evaporator:* The CSY-based evaporator (CSY-F) was woven on an SGA598 semi-automatic loom using a plain weave. CSYs served as warp yarns, threaded through the heddles and reed. PP/MXene yarns were used as weft yarns. The warp and weft densities were 30 and 200 yarns per 10 cm, respectively. Subsequently, a piece of plain weave CSY-F was formed.

*Characterization:* The microscopic morphology of samples was observed using a field-emission scanning electron microscope (FE-SEM, Sigma 500, Carl Zeiss AG, Germany). Crystal structures and phase compositions were analyzed through X-ray diffraction (XRD, Smarlab SE, Japan). The elemental composition of composite yarns was characterized through X-ray photoelectron spectroscopy (XPS, AXIS SUPRA+, Shimadzu, Japan). Optical transmittance and reflectance spectra of sample surfaces were measured using a UV–Vis–NIR spectrophotometer (UV-3600, Shimadzu, Japan) equipped with an integrating sphere. The absorbance ($A$) was calculated from reflectance ($R$) and transmittance ($T$) according to Kirchhoff's law: $A = 1 - R - T$. Infrared thermal distribution was recorded using a FLIR E8 thermal imaging camera (USA).

*Solar evaporation experiments:* *Preparation of simulated saline-alkali water solutions*—Saline-alkali water solutions with sodium ion concentrations of 50 mmol $L^{-1}$ and 150 mmol $L^{-1}$ were prepared to simulate low and high salinity–alkali stress conditions. The solutions were formulated with a molar ratio of NaCl:$Na_2SO_4$:$NaHCO_3$:$Na_2CO_3$ = 1:9:9:1 using reagent-grade chemicals.

*Solar evaporation system*—Solar steam generation experiments were conducted under controlled laboratory conditions of constant temperature and humidity. A xenon lamp solar simulator (HF-GHX-XE-300, Hefan) provided a consistent irradiance of 1 kW $m^{-2}$ (1 sun), verified using an optical power meter (MC-PM100C, Meiruichen). Mass loss due to evaporation was recorded every 10 s using an electronic balance with 0.0001 g precision.

## Acknowledgments

This work was supported financially by the Key Research and Development Program of Shaanxi (No. 2022ZDLSF01-11, No. 2024PT-ZCK-38), and the Technology Innovation Leading Program of Shaanxi, China (No. 2023KXJ-275).

## Conflict of Interest

The authors declare no conflict of interest.

## Data Availability Statement

The data that support the findings of this study are available in the Supporting Infomation of this article.

## Supporting Information

Supporting Information is available from the Wiley Online Library or from the author.


© 2026 The Author(s). *Energy & Environmental Materials* published by John Wiley & Sons Australia, Ltd on behalf of Zhengzhou University.

## Keywords

core-sheath structure, interfacial evaporator, saline-alkali water treatment, salt-alkali corrosion resistance, scalable preparation

Received: July 18, 2025
Revised: September 14, 2025
Published online: October 8, 2025

[1] Y. Huang, M. Deng, L. Li, Z. Wang, K. Song, F. Wu, *Environ. Sci. Technol.* **2025**, *59*, 3205.
[2] Z. Gao, X. Li, L. Zuo, B. Zou, B. Wang, W. J. Wang, *Remote Sens. Environ.* **2025**, *322*, 114708.
[3] J. Du, H. Xu, D. Zhang, S. Feng, *Nat. Commun.* **2025**, *16*, 4157.
[4] H. Shi, G. Luo, E. H. Sutanudjaja, O. Hellwich, X. Chen, J. Ding, S. Wu, X. He, C. Chen, F. U. Ochege, *Sci. Bull.* **2023**, *68*, 3240.
[5] P. Smith, R. M. Poch, D. A. Lobb, R. Bhattacharyya, G. Alloush, G. D. Eudoxie, L. H. Anjos, M. Castellano, G. M. Ndzana, C. Chenu, *Annu. Rev. Environ. Resour.* **2024**, *49*, 73.
[6] J. Thorslund, M. F. Bierkens, G. H. Oude Essink, E. H. Sutanudjaja, M. T. Van Vliet, *Nat. Commun.* **2021**, *12*, 4232.
[7] T. Wang, J. Jing, P. Huang, X. Guo, C. Li, Y. Qu, *J. Hazard. Mater.* **2025**, *488*, 137401.
[8] W. Zhao, J. Xiao, S. Wang, X. Gai, G. Chen, *Biochar* **2025**, *7*, 70.
[9] G. Zhang, L. Zhang, Z. Shi, Y. Yang, J. Liu, *Biochar* **2025**, *7*, 68.
[10] J. Ma, J. Du, H. Zhang, S. Li, Y. Jiang, F. Huang, *Chem. Eng. J.* **2025**, *509*, 161235.
[11] Q. Xiong, D. Wang, B. Shao, H. Yu, X. Wu, Y. Lu, X. Yang, H. Xu, *Adv. Funct. Mater.* **2025**, *35*, 2409257.
[12] S. Qi, T. Jia, Y. Zhang, Y. Zhao, Y. Xing, M. Zhang, F. Wang, C. Chen, W. Y. Wong, *Adv. Funct. Mater.* **2025**, *10*, 2503234.
[13] L. Hou, S. Li, Y. Qi, J. Liu, Z. Cui, X. Liu, Y. Zhang, N. Wang, Y. Zhao, *ACS Nano* **2025**, *19*, 9636.
[14] S. Stein, Y. Yechieli, E. Shalev, R. Kasher, O. Sivan, *Water Res.* **2019**, *156*, 46.
[15] H. Yu, H. Jin, M. Qiu, Y. Liang, P. Sun, C. Cheng, P. Wu, Y. Wang, X. Wu, D. Chu, *Adv. Mater.* **2024**, *36*, 2414045.
[16] B. Nie, Y. Meng, S. Niu, L. Gong, Y. Chen, L. Guo, X. Li, Y. Wu, H. Li, W. Zhang, *Energy Environ. Sci.* **2025**, *18*, 3870.
[17] Y. Xiao, H. Guo, M. Li, J. He, X. Xu, S. Liu, L. Wang, T. D. James, *Coord. Chem. Rev.* **2025**, *527*, 216378.
[18] H. Jiang, X. Liu, D. Wang, Z. Qiao, D. Wang, F. Huang, H. Peng, C. Hu, *J. Energy Chem.* **2023**, *79*, 581.
[19] M. S. Irshad, I. Ahmed, N. Arshad, M. Alomar, Y. Shu, G. Zhenzhen, S. Ahmad, I. Zuburtikudis, S. Ruiqing, T. Mei, *Adv. Sci.* **2025**, *12*, 2415101.
[20] J. Jang, D. Kim, J. Park, H. Lim, H. Choi, S. Jung, D. Lee, G. Kwon, C. Wang, I. Cho, *Small* **2025**, *21*, 2409014.
[21] J. Zhang, K. Yang, B. Zhang, J. Wang, X. Yu, X. Lu, X. Lei, R. Fang, *Desalination* **2024**, *592*, 118173.
[22] B. Fu, X. Zhang, N. Robinson, Z. Zhang, J. Zhang, J. Ji, Y. Xu, K. Zhang, M. Dong, J. Kang, *Nano Energy* **2024**, *129*, 110054.
[23] S. Li, H. Zhang, S. Li, J. Wang, Q. Wang, Z. Cheng, *Renew. Sust. Energ. Rev.* **2024**, *202*, 114641.
[24] J. Luo, R. Qiao, B. Ding, *Matter* **2024**, *7*, 3351.
[25] R. Ghanbari, E. N. Zare, *Coord. Chem. Rev.* **2024**, *518*, 216089.
[26] J. Kang, M. A. Hickner, G. M. Geise, C. Nam, *Chem. Eng. J.* **2025**, *507*, 160350.
[27] Y. Cao, P. Gong, P. Yu, Y. Wang, Z. Zuo, C. Pan, X. Wang, P. Zhong, X. Ma, *Chem. Eng. J.* **2025**, *505*, 159742.
[28] R. Zhao, X. Chen, X. Chen, P. Zhang, C. Luo, P. Zhang, M. Chao, L. Yan, *J Mater Chem A* **2025**, *13*, 5684.
[29] J. Sun, M. U. Farid, W. Xi, G. Lu, M. W. Boey, S. K. Ravi, P. H. L. Sit, A. K. An, *Adv. Funct. Mater.* **2025**, *12*, 2416768.
[30] X. Ouyang, P. Wu, J. Deng, Q. Ma, X. Dong, W. Yu, G. Liu, J. Wang, L. Liu, *Sep. Purif. Technol.* **2022**, *297*, 121523.
[31] Q. Xie, S. Deng, Y. Wen, Y. Yang, W. Fu, J. Liu, S. Cheng, *Chem. Eng. J.* **2024**, *500*, 157434.
[32] H.-W. Kim, T. Yun, S. Hong, S. Lee, S. Jeong, *Water Res.* **2020**, *175*, 115677.
[33] H. Dou, J. Bai, H. Lu, T. Zhang, L. Kong, Z. Bai, W. Li, *Cement Concrete Comp.* **2023**, *136*, 104861.
[34] C. Zhang, Z. Zhu, S. Wang, J. Zhang, *Constr. Build. Mater.* **2023**, *368*, 130365.
[35] M. G. Abouelenein, M. M. Abdeen, O. A. El-Shamy, Q. Mohsen, M. Deyab, *Electrochim. Acta* **2025**, *514*, 145675.
[36] D. Wang, R. Zhu, X. Tang, J. Y. Tan, H. Li, Y. Chen, Z. Lin, X. Xia, S. Fu, *Adv. Fiber Mater.* **2025**, *7*, 748.
[37] H. Xie, X. Li, J. Hu, M. Pazuki, M. Salimi, H. Li, L. Zhang, M. Amidpour, Z. Chen, *Desalination* **2025**, *601*, 118579.
[38] L. Wu, S. Guan, W. Si, B. Zhou, J. Wang, S. Guo, G. Zhu, M. Wang, G. J. H. Melvin, H. Ogata, *Sep. Purif. Technol.* **2025**, *362*, 131736.
[39] X. Chen, S. He, M. M. Falinski, Y. Wang, T. Li, S. Zheng, D. Sun, J. Dai, Y. Bian, X. Zhu, *Energy Environ. Sci.* **2021**, *14*, 5347.
[40] J. Sun, Y. Xin, T. Sun, B. Sun, Y. Yang, Q. Yang, X. Fan, *Chem. Eng. J.* **2024**, *501*, 157740.
[41] C. Shi, P. Zhang, Y. Wang, K. Zhang, J. Chen, X. Li, H. Jin, Y. Wang, C. Yan, Y. Shi, *Adv. Funct. Mater.* **2025**, *9*, 2501165.
[42] C. Zhang, Y. Shi, L. Shi, H. Li, R. Li, S. Hong, S. Zhuo, T. Zhang, P. Wang, *Nat. Commun.* **2021**, *12*, 998.
[43] Y. Wu, C. Ma, K. Zhu, L. Jin, L. Song, L. Li, Y. Lu, Y. Zheng, Y. Zhang, X. Zheng, *Energy Environ. Sci.* **2024**, *17*, 9303.
[44] Y. Xia, Q. Hou, H. Jubaer, Y. Li, Y. Kang, S. Yuan, H. Liu, M. W. Woo, L. Zhang, L. Gao, *Energy Environ. Sci.* **2019**, *12*, 1840.
[45] R. Xu, P. Luo, H. Zhao, H. Lu, T. Zhou, *J Mater Chem A* **2025**, *13*, 12611.
[46] Y. Chen, R. Zhou, H. Wang, X. Ning, Y. Du, H. Xie, T. Wu, J. Qu, *J. Energy Chem.* **2025**, *105*, 385.
[47] T. Zhai, X. Li, Z. Chen, Y. Peng, M. Salimi, L. Zhang, M. Amidpour, Z. Chen, *Chem. Eng. J.* **2025**, *506*, 159892.
[48] F. Xia, Y. Tian, X. Zhang, Y. Gong, X. Yang, X. Guo, S. Yang, Y. Hu, X. Xu, R. Zhou, *ACS Nano* **2025**, *19*, 8608.
[49] L. Zhao, L. Zhang, Z. Yang, T. Zhou, P. Cao, L. Chen, Y. Zhang, T. Qin, Z. Yong, K. Wu, *Chem. Eng. J.* **2024**, *490*, 151605.
[50] J. Li, K. Hua, H. Qiao, Y. Yao, D. Xu, Z. Zhang, J. He, W. Li, J. Li, *Chem. Eng. J.* **2025**, *507*, 160746.
[51] X. Xiao, L. Pan, T. Chen, M. Wang, L. Ren, B. Chen, Y. Wang, Q. Zhang, W. Xu, *Engineering* **2023**, *30*, 153.
[52] L. Yang, X. Chen, Z. Lv, C. Luo, M. Chao, P. Zhang, L. Yan, *Sep. Purif. Technol.* **2024**, *348*, 127525.
[53] W. Liu, Y. Wang, Q. Chen, J. Wu, N. Meng, Y. Liao, *ACS Sustain. Chem. Eng.* **2025**, *25*, 9370.
[54] Y. Wang, F. Chen, Q. Chen, W. Liu, Q. Huang, X. Hou, S. Li, C. Cheng, X. Xie, N. Meng, *Nat. Commun.* **2025**, *16*, 6373.
[55] H. Sang, C. Tang, K. Ma, X. Li, *J Water Process Eng* **2023**, *56*, 104403.
[56] X. Jiang, C. Tang, X. Li, Z. Chen, *Chem. Eng. J.* **2025**, *521*, 166473.
[57] Q. Wan, P. Xiang, C. Tang, X. Li, Z. Chen, *Chem. Eng. J.* **2025**, *515*, 163551.
[58] H. Shu, H. Sang, C. Tang, K. Ma, X. Li, *Chem. Eng. J.* **2025**, *506*, 160060.
[59] P. Xiang, C. Tang, K. Ma, X. Li, *Desalination* **2025**, *594*, 118281.
[60] F. Yu, C. Luo, X. Niu, M. Chao, P. Zhang, L. Yan, *Nano Res* **2024**, *17*, 2368.
[61] Z. Lv, X. Chen, L. Yang, M. Li, C. Xia, C. Luo, M. Chao, L. Yan, *ACS Appl. Polym. Mater.* **2024**, *6*, 6347.
[62] L. Li, C. Luo, X. Chen, N. Chu, L. Li, M. Chao, L. Yan, *Adv. Funct. Mater.* **2023**, *33*, 2213974.
[63] Y. Zhang, X. Chen, C. Luo, J. Gu, M. Li, M. Chao, X. Chen, T. Chen, L. Yan, X. Wang, *Adv. Funct. Mater.* **2022**, *32*, 2111660.


© 2026 The Author(s). *Energy & Environmental Materials* published by John Wiley & Sons Australia, Ltd on behalf of Zhengzhou University.

[64] S. Zhang, M. Li, C. Jiang, D. Zhu, Z. Zhang, *Adv. Sci.* **2024**, *11*, 2308665.
[65] J. Ma, X. Sun, L. Wang, M. An, M. Kim, Y. Yamauchi, N. Khaorapapong, Z. Yuan, *Nano Energy* **2025**, *137*, 110781.
[66] M. Zou, Y. Zhang, Z. Cai, C. Li, Z. Sun, C. Yu, Z. Dong, L. Wu, Y. Song, *Adv. Mater.* **2021**, *33*, 2102443.
[67] Y. Zhu, Y. Chen, P. Ma, H. Xing, J. Fan, X. Deng, Y. Liu, L. Lin, Q. Zheng, *Chem. Eng. J.* **2025**, *514*, 163410.
[68] B. Wang, C. Wang, Y. Li, J. Jin, X. Lin, C. Shi, *Energy Environ. Sci.* **2025**, *18*, 3432.
[69] X. Li, Z. Zhang, X. Zhang, Y. Cao, Y. Yang, W. Wang, J. Wang, *Adv. Sci.* **2024**, *11*, 2308200.
[70] M. Jing, W. Wang, Y. Fu, Y. Yang, W. Song, Z. Sun, *Desalination* **2023**, *564*, 116792.
[71] L. Mi, Z. Zhang, X. Zhang, C. Han, W. Wang, W. Song, Z. Sun, *J Mater Chem A* **2023**, *11*, 21577.
[72] Z. Sun, C. Han, S. Gao, Z. Li, M. Jing, H. Yu, Z. Wang, *Nat. Commun.* **2022**, *13*, 5077.
[73] Y. Lu, D. Li, F. Liu, *Materials* **2022**, *15*, 307.
[74] T. Wang, M. Li, H. Xu, X. Wang, M. Jia, X. Hou, S. Gao, Q. Liu, Q. Yang, M. Tian, *Nano-Micro Lett.* **2024**, *16*, 220.
[75] Z. Zhan, Y. Su, M. Xie, Y. Li, Y. Shuai, Z. Wang, *Mater. Today* **2024**, *80*, 529.
[76] Q. Zhang, G. Yi, Z. Fu, H. Yu, S. Chen, X. Quan, *ACS Nano* **2019**, *13*, 13196.
[77] B. Liu, L. Yu, F. Yu, J. Ma, *Desalination* **2021**, *500*, 114897.
[78] Y. Wang, Y. Wan, X. Meng, L. Jiang, H. Wei, X. Zhang, N. Ma, *J. Mater. Sci.* **2022**, *57*, 13962.
[79] Z. Zheng, H. Liu, D. Wu, X. Wang, *Chem. Eng. J.* **2022**, *440*, 135862.
[80] Z. Yu, P. Wu, *Adv. Mater. Technol.* **2020**, *5*, 2000065.
[81] Y. Yang, W. Fan, S. Yuan, J. Tian, G. Chao, T. Liu, *J Mater Chem A* **2021**, *9*, 23968.
[82] H. Gao, N. Bing, Z. Bao, H. Xie, W. Yu, *Chem. Eng. J.* **2023**, *454*, 140362.
[83] X. Ming, A. Guo, Q. Zhang, Z. Guo, F. Yu, B. Hou, Y. Wang, K. P. Homewood, X. Wang, *Carbon* **2020**, *167*, 285.
[84] X. Han, S. Ding, L. Fan, Y. Zhou, S. Wang, *J Mater Chem A* **2021**, *9*, 18614.


© 2026 The Author(s). *Energy & Environmental Materials* published by John Wiley & Sons Australia, Ltd on behalf of Zhengzhou University.